Role of the Crystal Lattice Structure in Predicting Fracture Toughness

Thuy Nguyen[1,2] and Daniel Bonamy[1,*]
[1]Service de Physique de l'Etat Condensée, CEA, CNRS, Université Paris-Saclay, CEA Saclay 91191 Gif-sur-Yvette Cedex, France
[2]EISTI, Université Paris-Seine, Avenue du Parc, 95000 Cergy Pontoise Cedex, France

(Received 20 May 2019; revised manuscript received 30 August 2019; published 15 November 2019)

We examine the atomistic scale dependence of a material's resistance to failure by numerical simulations and analytical analysis in electrical analogs of brittle crystals. We show that fracture toughness depends on the lattice geometry in a way incompatible with Griffith's relationship between fracture and free surface energy. Its value finds its origin in the matching between the continuum displacement field at the engineering scale, and the discrete nature of solids at the atomic scale. The generic asymptotic form taken by this field near the crack tip provides a solution for this matching, and subsequently a way to predict toughness from the atomistic parameters with application to graphene.

DOI: 10.1103/PhysRevLett.123.205503

Predicting when failure occurs is central to many industrial, societal, and geophysical fields. For brittle solids under tension, the problem reduces to the destabilization of a preexisting crack: Remotely applied stresses are dramatically amplified at the crack tip, and all the dissipation processes involved in the problem are confined in a small fracture process zone (FPZ) around this tip. Linear elastic fracture mechanics (LEFM) provides the framework to describe this stress concentration; the main result is that the near-tip stress field exhibits a square-root singularity fully characterized by a single parameter, the stress intensity factor, K [1,2]. Crack destabilization is governed by the balance between the flux of the mechanical energy released from the surrounding material into the FPZ and the dissipation rate in this zone. The former is computable via elasticity and connects to K. The latter is quantified by the fracture energy Γ required to expose a new unit area of cracked surface [3]. Equivalently, it can be quantified by the fracture toughness K_c, which is the K value above which the crack starts propagating. Both quantities are related via Irwin's formula [4],

$$K_c = \sqrt{E\Gamma}, \tag{1}$$

where E is Young's modulus.

Within LEFM theory, both Γ and K_c are material constants, to be determined experimentally. Still, their value is governed by the various dissipation processes (viscous or plastic deformations, crazing, etc.) at play in the FPZ. As such, it should be possible to infer Γ and K_c from the knowledge of the atomistic parameters, at least for perfectly brittle crystals in which cleavage occurs via successive bond breaking, without involving further elements of dissipation. In Griffith's seminal work [3], he proposed to relate Γ to the free surface energy per unit area γ_s, which is the bond energy times the number of bonds per unit surface:

$$\Gamma = 2\gamma_s. \tag{2}$$

The factor two, here, comes from the fact that breaking one bond creates two surface atoms. This formula significantly underestimates Γ [5–8]. A major hurdle is to conciliate the continuum LEFM description with the discrete nature of solids at the atomic scale: Lattice trapping effect has, e.g., been invoked [9–14] to explain the observed shift in Griffith threshold. Analytical analysis of crack dynamics in lattices has also evidenced [15,16] novel high frequency waves, nonexistent in the elastic continuum, which may also explain the anomalously high value of Γ [17]. Still, until now, predicting fracture energy remains elusive.

Here, we examined how the material's resistance to crack growth is selected in two-dimensional (2D) fuse lattices of different geometries. These model digital materials, indeed, both possess perfectly prescribed and tunable "atomic bonds" and satisfy isotropic linear elasticity under antiplane deformation at the continuum scale [18–21]. Fracture energy is observed to be significantly larger than Griffith's prediction, by a factor depending on the lattice geometry. It is the fine positioning of continuum stress or displacement fields onto the discrete lattice which sets the value of K_c, and consequently that of Γ. We demonstrate how the singular form of these fields near the crack tip constrains this positioning, and subsequently permits us to predict fracture toughness not only in simplified antiplanar elasticity, but also in genuine elastic problems, with an application to graphene.

Numerics.—Rectangular fuse lattices of size $2L \times L$ in the x and y directions were created and a horizontal straight crack of initial length $4L/5$ is introduced from the

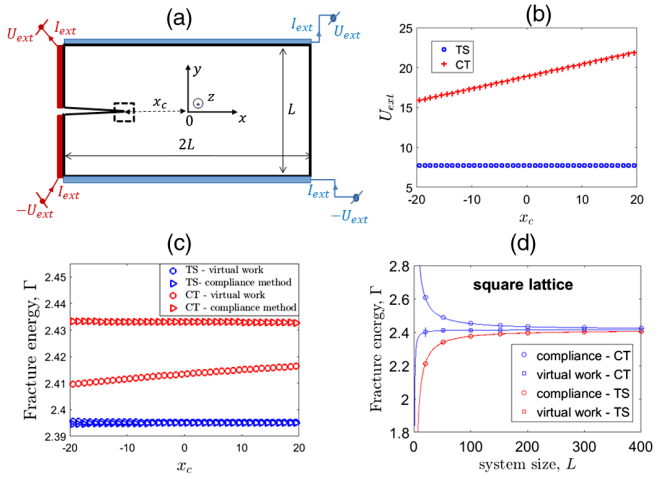

FIG. 1. (a) Sketch and notation of the simulated fuse lattice. The external voltage difference $2U_{\text{ext}}$ is imposed between the blue electrodes in the TS configuration, and between the red ones in the CT configuration. In response, a total current I_{ext} flows through the network. U_{ext} and I_{ext} are the analog of loading displacement and loading force in experimental mechanics. (b) U_{ext} value at breaking onset as a function of crack tip position x_c, in a 200×100 square lattice. (c) Γ vs x_c in the same system. Note that the y axis ranges from 2.39 to 2.46. Γ is nearly independent of x_c, no matter how it is measured and the loading configuration. (d) Size dependency of Γ averaged over x_c. For small sizes, Γ depends on both the measurement method and loading configuration. However, the differences vanish as $L \to \infty$. All curves were fitted by $\Gamma = a/L^p + \Gamma_\infty$, and the fitted value Γ_∞ is a material constant, independent of both the loading configuration and measurement method. Panel (d) concerns the square geometry but the same features were observed in triangular and honeycomb lattices. Table I (third line) provides the values Γ measured in the three lattice geometries.

left-handed side in the middle of the strip, by withdrawing the corresponding bonds [Fig. 1(a)]. This fuse network is an electrical analog of an elastic plate under antiplanar loading, where voltage field $u(x, y)$ formally maps to out-of-plane displacement, $\mathbf{u}(x, y) = u(x, y)\mathbf{e}_z$. Triangular, square, and honeycomb geometries were considered; they lead to different values for E and γ_s (Table I, see Supplemental Material [22] for derivation details). The length, conductance, and current breakdown threshold for each fuse were assigned to unity: $\ell = 1$, $g = 1$, and $i_c = 1$ and all quantities thereafter are given in reduced units: ℓ unit for length, g for stresses, $i_c^2/g\ell$ for surface or fracture energy, and $i_c/\sqrt{\ell}$ for stress intensity factor or fracture toughness.

Two different loading schemes were imposed: Thin strip (TS) configuration where the voltage difference $2U_{\text{ext}}$ is applied between the top and bottom nodes of the lattice, and compact tension (CT) configuration in which the voltage difference is applied between the upper (above crack) and lower (below crack) part of the left-handed side [Fig. 1(a)]. Voltages at each node and currents in each fuse were determined so that Kirchhoff's and Ohm's law are satisfied everywhere. For both schemes, U_{ext} was increased until the current flowing through the fuse right at the crack tip reached i_c; this point corresponds to the crack destabilization. This fuse was withdrawn, the crack advanced one step, and so on. The procedure was repeated until the crack has grown an additional length of $2L/5$; at each step, the tip abscissa x_c was located at the center of mass of the next fuse about to burn.

$\Gamma(x_c)$ was computed using two procedures: (i) the virtual work method, where Γ was computed from the loss of total energy stored in the lattice ($E_{\text{total}} = \sum_p i_p^2/2g$, where the current i_p flows through fuse p) as the crack fuse is burned, keeping U_{ext} constant; (ii) the compliance method, where $G(x_c) = (1/2)(2U_{\text{ext}})^2 dG_{\text{glob}}/dx_c$ is computed from the x_c variation of the global lattice conductance, [$G_{\text{glob}} = I_{\text{ext}}/2U_{\text{ext}}$ where I_{ext} is the total current flowing through the lattice, see Fig. 1(a)]. The latter is widely used in experimental mechanics [24] since it relates fracture energy to continuum-level scale quantities only.

Results.—Figure 1(b) displays examples of the profiles $U_{\text{ext}}(x_c)$ obtained in both TS and CT loading configurations: U_{ext} is independent of x_c in the first case, and increases with x_c in the second case. Conversely, Γ is nearly constant, within less than 0.5%. In-depth examination actually reveals slight dependencies with the measurement method and loading conditions [Fig. 1(c)]. The differences are significant in small systems, but they decrease with increasing L [Fig. 1(d)]. In the continuum limit ($L \to \infty$), all values converge toward the same material constant limit Γ_∞, as expected in LEFM. From now on, the ∞ subscript is dropped for the sake of simplicity. Table I (third line) reports the continuum-level scale values in the three lattice geometries considered here. In all cases, they are larger than Griffith's prediction [Eq. (2)], by a factor ranging between 1.75 to 3.67 depending on the geometry.

To understand the selection of Γ, we turned to the analysis of the spatial distribution of voltage [Fig. 2(a)]. Williams showed [25] that, in a continuum elastic body embedding a slit crack, the displacement field writes as a series of elementary solutions Φ_n,

$$u(r, \theta) = \sum_{n \geq 0} a_n \Phi_n(r, \theta). \tag{3}$$

Here, r is the distance to the crack tip and θ is the angle with respect to the crack line. In the antiplane (mode III) crack problem examined here, Φ_n write (Supplemental Material [22])

$$\Phi_n^{\text{III}}(r, \theta) = \begin{cases} r^{n/2} \sin \frac{n\theta}{2} & \text{if } n \text{ odd} \\ 0 & \text{otherwise.} \end{cases} \tag{4}$$

The term $n = 1$ is the usual square root singular term and a_1 relates to K via $K = Ea_1\sqrt{2\pi}/4$ (see, e.g., Ref. [1]).

TABLE I. Synthesis of the different elastic and fracture parameters at play in the three lattice geometries examined here.

Lattice geometry	Square	Triangular	Honeycomb
E (g)	2	$2\sqrt{3}$	$2/\sqrt{3}$
$2\gamma_s$ $(i_c^2/g\ell)$	1	2	$1/\sqrt{3}$
Γ (sim) $(i_c^2/g\ell)$	2.414 ± 0.002	3.512 ± 0.012	2.152 ± 0.012
K_c (sim) $(i_c/\sqrt{\ell})$	2.198 ± 0.011	3.489 ± 0.007	1.576 ± 0.008
K_c (approx. theo.) $(i_c/\sqrt{\ell})$	2.19	3.55	1.40
K_c (exact theo.) $(i_c/\sqrt{\ell})$	2.24734	3.57137	1.59697

Equations (3) and (4), truncated to the first six terms ($n \leq 11$), were used to fit $u(r,\theta)$ obtained in the numerical experiments. A difficulty here is to place properly the crack tip in the lattice; as a first guess, this tip is located in the center of the next bond to break [Fig. 2(b)]. The fitted field is in good agreement with the measured one, except in the very vicinity of the crack tip [Fig. 2(c)]. Unfortunately, this near-tip zone is precisely the one setting whether or not the next bond breaks.

The near-tip discrepancy above results from the mismatch problem between the continuum fields of LEFM and the lattice discreteness at small scale, yielding a crack tip mispositioning. A similar problem has been faced in experimental mechanics to find out the crack tip on samples, knowing the displacement field at a set of discrete points via digital image correlation [26]. This problem was solved by noting that the elementary solutions Φ_n in the Williams expansion obey [27,28] $\partial\Phi_n/\partial x = n\Phi_{n-2}/2$. Then, a slight mispositioning of the tip position x by a small distance d leads to an additional, super-singular ($n = -1$), term in Eq. (3), with a prefactor $a_{-1} \simeq a_1 d/2$ [26]. The crack tip can then be located as follows: (i) Start with an arbitrary mispositioned origin (in the center of the next bond to break in our case); (ii) fit the displacement field with Eq. (3) to which the super-singular ($n = -1$) term has been added; (iii) correct the origin position by shifting it by $d = 2a_{-1}/a_1$; and (iv) repeat this process [steps (ii) and (iii)] until the shifting distance d is less than a prescribed value (0.01ℓ in our case). Herein, this convergence occurred in less than 3 iterations, irrespectively of the lattice geometry, lattice size and loading scheme. The obtained displacement fields fit now that measured numerically extremely well, even in the very vicinity of the crack tip [Fig. 2(d)]. The value of K_c arises from the fitting parameter a_1. K_c depends on L for small sizes, in a way depending whether CT or TS configurations are applied. However, as Γ, K_c converges toward a constant, loading independent value as $L \to \infty$ [Fig. 3]. The convergence is faster in lattices with higher symmetry. It also depends on loading conditions in the case with the highest symmetry (triangular lattice). Table I (fourth line) provides the asymptotic values obtained in the square, honeycomb, and triangular geometries. In all cases, Irwin's formula [Eq. (1)] relating K_c and Γ is properly satisfied, within 0.8%.

Is it now possible to predict fracture toughness from scratch in the different lattices, without resorting to simulations? To do so, we use the singular nature of the near-tip field and make $L \to \infty$. Consider now the very vicinity of the next bond about to break, call **A** and **B** the two edge atoms, and position, as a first guess, the crack tip at the center **O** of this bond [Fig. 2(b)]. All the $n > 1$ terms vanish in the Williams expansion and the voltage field, there, is fully characterized by two unknown only: the singular term prefactor a_1 and the super-singular one a_{-1}.

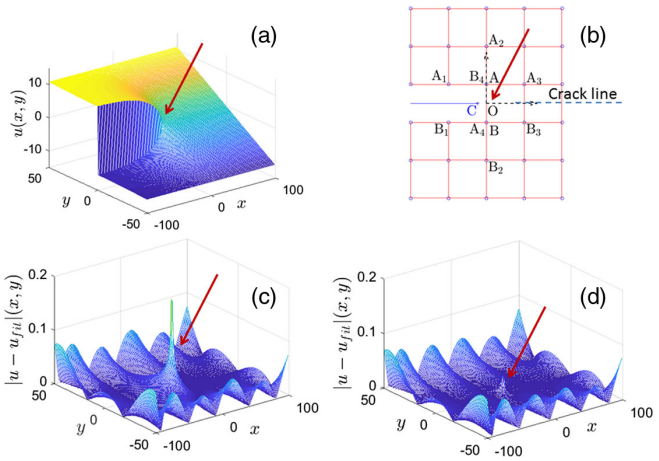

FIG. 2. Spatial distribution of the voltage field and the effect of crack-tip mispositioning. (a) Map of voltage field, $u(x,y)$ in a 200×100 square lattice under TS loading. The crack lies along x in the middle of the strip, so that the next bond about to break is at the map center (red arrow) and the external applied voltage difference $2U_{\text{ext}}$ is at the value required to break this bond. Equations (3) and (4) are expected to describe this field. (b) Zoom on the tip vicinity emphasizing the lattice discreetness. The difficulty is to place the continuum-scale crack tip in this discrete lattice. At first, this tip is placed in the middle, **O**, of the bond to break. (c) The absolute difference $|u_{\text{fit}} - u|(x,y)$ between the voltage field of panel (a) and the one $u_{\text{fit}}(x,y)$ fitted using Eqs. (3) and (4), with $1 \leq n \leq 11$ (6 terms). The fit is very good everywhere, except in the very vicinity of the crack tip (red arrow). (d) Absolute difference $|u_{\text{fit}} - u|(x,y)$ after correcting for the mispositioning and placing the continuum-scale tip at the proper position **C**, using the iterative procedure depicted in the text. The fit is now very good everywhere.

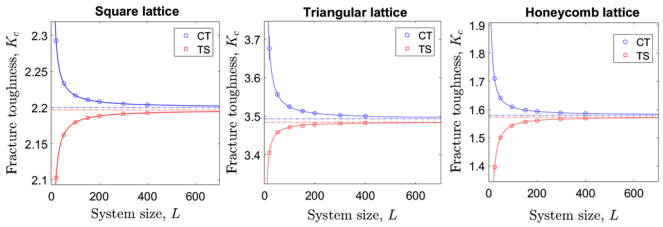

FIG. 3. Fracture toughness K_c plotted as a function of the system size L, in both the TS and CT loading configurations, for the three lattice geometries: square, honeycomb, and triangular. K_c is obtained by fitting the voltage field $u(x,y)$ using Eqs. (3) and (4) after having corrected the tip mispositioning using the iterative procedure depicted in the main text. For all curves, the continuous line is a power-law fit $K_c = a/L^p + K_c^\infty$. The material constant K_c^∞ obtained in the thermodynamic limit ($L \to \infty$) is independent of the loading conditions (dotted horizontal lines). These values are reported in the fourth line of Table I.

Their values are then determined by the Kirchhoff laws at $\mathbf{A}$ (or equivalently at $\mathbf{B}$): $\sum_i [u(\mathbf{A}_i) - u(\mathbf{A})] = 0$, where $\mathbf{A}_i$ are the nodes themselves in contact with $\mathbf{A}$. This equation gives a_{-1}/a_1, and, subsequently, an approximation of the distance d between $\mathbf{O}$ and the true position $\mathbf{C}$ of the effective continuum-level scale crack tip [Fig. 2(b)]

$$d = -2\frac{\sum_i [\Phi_1^{\mathrm{III}}(r_{\mathbf{A}_i}, \theta_{\mathbf{A}_i}) - \Phi_1^{\mathrm{III}}(r_{\mathbf{A}}, \theta_{\mathbf{A}})]}{\sum_i [\Phi_{-1}^{\mathrm{III}}(r_{\mathbf{A}_i}, \theta_{\mathbf{A}_i}) - \Phi_{-1}^{\mathrm{III}}(r_{\mathbf{A}}, \theta_{\mathbf{A}})]}. \tag{5}$$

Shifting the reference frame origin from $\mathbf{O}$ to $\mathbf{C}$ leads to the disappearance of the super-singular term. Furthermore, the prefactor of the singular term is equal to $a_1 = 4K_c/E\sqrt{2\pi}$ when the force $i_{AB} = u(\mathbf{B}) - u(\mathbf{A})$ applying to the bond $\mathbf{A} - \mathbf{B}$ is equal to the breaking threshold $i_c = 1$. This yields

$$K_c = \frac{E\sqrt{\pi}}{2[\Phi_1^{\mathrm{III}}(\tilde{r}_{\mathbf{A}}, \tilde{\theta}_{\mathbf{A}}) - \Phi_1^{\mathrm{III}}(\tilde{r}_{\mathbf{B}}, \tilde{\theta}_{\mathbf{B}})]}, \tag{6}$$

where $(\tilde{r}, \tilde{\theta})$ are the polar coordinate of the considered point in the new reference frame positioned at $\mathbf{C}$. Equations (5) and (6) provide an approximation for K_c in the three lattice geometries considered here. The values are reported in Table I (fifth line) and coincide with that measured on the numerical experiments within 1%, 11%, and 2% for square, honeycomb, and triangular lattices, respectively.

Note that the mispositioning d obtained by Eq. (5) is an approximation only since it involves Kirchhoff's law at a single point $\mathbf{A}$ and a single iteration in the shifting procedure. Actually, both assumptions can be released by imposing Kirchhoff laws to an arbitrary number of nodes and by applying more iterations. These refinements are described in the Supplemental Material [22]. They provide *ab initio* predictions for the fracture toughness, up to any prescribed accuracy. Table I (sixth line) presents the obtained values. They coincide with the numerically measured ones within 2%, 1.3%, and 2% for square, honeycomb, and triangular lattices, respectively.

The analytical procedure derived here for model electric or scalar elastic crack problems can be extended to genuine 2D elastic (plane stress) crack problems. This comes about via several correspondences: (i) In such cases, the (vectorial) displacement field $\mathbf{u}(x,y)$ also follows Williams's asymptotic form [Eq. (3)]; and (ii) the relation $\partial \mathbf{\Phi}_n^I/\partial x = n\Phi_n^I/2$ remains valid [26]. Here, superscript I indicates opening fracture mode (mode I). Nevertheless, 2D crystals include an additional complicating element with respect to the fuse networks considered until now: the deformations are accommodated at the atomistic scale by two distinct modes: bond stretching and bond bending, characterized by the bond stretching stiffness k_s and bond bending stiffness k_b [both can be measured experimentally via infrared spectroscopy [29]]. The procedure then follows the same route as for the electrical network; it is detailed in the Supplemental Material [22]. It quantitatively relates K_c to E, k_s, k_b, ℓ, the bond strength F_c, the Poisson ratio ν and the crystal geometry. This procedure has been applied in graphene, which has a planar honeycomb geometry with $\ell = 0.142$ nm and $E = 340\ \mathrm{N\,m^{-1}}$ [30], $\nu = 0.18$ [31], $k_s \simeq 688$–$740\ \mathrm{N\,m^{-1}}$ [32], $k_b = 0.769$–$0.776 \times 10^{-18}\ \mathrm{N\,m\,rad^{-2}}$ [32], and $F_c = 13.6$ nN [33]. It yields $K_c = 1.25 \times 10^{-3}\ \mathrm{N\,m^{-1/2}}$ (Supplemental Material [22]). Fracture energy is subsequently deduced from Irwin's formula [Eq. (1)]: $\Gamma = 4.6 \times 10^{-9}\ \mathrm{J\,m^{-1}}$. The predicted values for K_c and Γ are very close to the experimental ones [34]: $K_c = 1.4 \times 10^{-3}\ \mathrm{N\,m^{-1/2}}$ and $\Gamma = 5.4 \times 10^{-9}\ \mathrm{J\,m^{-1}}$. Note that Griffith's seminal prediction [Eq. (2)] would have yielded $\Gamma = (1/2\sqrt{3})(F_c^2/k_s\ell) \simeq 5.08$–$5.47 \times 10^{-10}\ \mathrm{J\,m^{-1}}$; hence it underestimates the measured value by a factor of 10.

Concluding discussion.—This work demonstrates the key role played by the crystal lattice geometry at the atomistic scale in the selection of the resistance to failure at the macroscopic scale. It challenges Griffith's seminal interpretation [3] directly linking Γ to γ_s. It also questions the argument proposed in Refs. [15–17] to explain Griffith's failure: Slepyan *et al.* examined the structure of the waves emitted when cracks propagate in discrete lattices at constant speed v and, from this, they determined the fracture energy and its variation with v, $\Gamma(v)$. They observed that in the limit of vanishing speed, $\Gamma(v \to 0^+)$ is larger than $2\gamma_s$. They attributed the difference to the energy of phonons (lattice-induced high-frequency waves) that would survive when $v = 0$. Inertia is absent in our simulations and, hence, phonons cannot be activated. Still, we observe the same anomalously high value for fracture energy, as that obtained in dynamically cracking lattices at vanishing speeds; it is worth mentioning that the value 2.414 determined here for a square lattice (Table I) coincides exactly with that reported in Ref. [15] in the $v \to 0$ limit. This means that the fracture energy in excess does not find its origin in the presence of phonons as argued

in Refs. [15–17]. The interpretation we propose is that fracture toughness is fixed by the fine positioning of the near tip singularity of the continuum stress field on the crystal lattice, then by its adjustment so that the force exerted on a chemical bond is sufficient to break it. Then *in a second step*, fracture energy is deduced from Irwin's formula [Eq. (1)].

Quantitative predictions for fracture toughness have been reached here for bidimensional crystals. The analysis is expendable to 3D and nonlinear cases. This necessitates to use the proper (and more complicated) asymptotic near-tip displacement fields, e.g., those obtained in anisotropic elasticity for 3D crystals, the asymptotic HRR solutions [35,36] for power-law hardening solids, or those obtained in weakly nonlinear elasticity, in Ref. [37]. The analysis can also be instrumental to explain how fracture toughness evolves with relative density and/or stockiness in cellular materials of various geometries [38–41]. Finally, it may catalyze further research toward novel tough, lightweight metamaterials. In this context, the use of microlattices made from periodically arranged hollow microtubes seems extremely promising [42–44]; they both exhibit ultralow densities and good resistance to compressive fracture. Our Letter provides the first step to address tensile fracture in this novel class of metamaterials. Beyond solid fracture, the analysis presented here may aid in the progression and understanding of a variety of singularity-driven systems, including the selection of the slip length in the wetting contact line problem [45] and the selection of the dislocation core size in crystal plasticity.

We thank Francois Daviaud, Francois Ladieu, and Cindy Rountree for the careful reading of the manuscript. Funding through ANR project MEPHYSTAR (ANR-09-SYSC-006-01) and by "Investissements d'Avenir" LabEx PALM (ANR-10-LABX-0039-PALM) is also gratefully acknowledged.

*Daniel.Bonamy@cea.fr

[1] B. Lawn, *Fracture of Brittle Solids* (Cambridge University Press, Cambridge, 1993).
[2] D. Bonamy, Dynamics of cracks in disordered materials, C.R. Phys. **18**, 297 (2017).
[3] A. A. Griffith, The phenomena of rupture and flow in solids, Phil. Trans. R. Soc. A **221**, 163 (1921).
[4] G. R. Irwin, Analysis of stresses and strains near the end of a crack traversing a plate, J. Appl. Mech. **24**, 361 (1957).
[5] R. Pérez and P. Gumbsch, Directional Anisotropy in the Cleavage Fracture of Silicon, Phys. Rev. Lett. **84**, 5347 (2000).
[6] T. Zhu, J. Li, and S. Yip, Atomistic Study of Dislocation Loop Emission from a Crack Tip, Phys. Rev. Lett. **93**, 025503 (2004).
[7] M. J. Buehler, H. Tang, A. C. T. van Duin, and W. A. Goddard, Threshold Crack Speed Controls Dynamical Fracture of Silicon Single Crystals, Phys. Rev. Lett. **99**, 165502 (2007).
[8] J. R. Kermode, A. Gleizer, G. Kovel, L. Pastewka, G. Csányi, D. Sherman, and A. De Vita, Low Speed Crack Propagation Via Kink Formation and Advance on the Silicon (110) Cleavage Plane, Phys. Rev. Lett. **115**, 135501 (2015).
[9] R. Thomson, C. Hsieh, and V. Rana, Lattice trapping of fracture cracks, J. Appl. Phys. **42**, 3154 (1971).
[10] C. Hsieh and R. Thomson, Lattice theory of fracture and crack creep, J. Appl. Phys. **44**, 2051 (1973).
[11] M. Marder and S. Gross, Origin of crack tip instabilities, J. Mech. Phys. Solids **43**, 1 (1995).
[12] M. Marder, Statistical mechanics of cracks, Phys. Rev. E **54**, 3442 (1996).
[13] N. Bernstein and D. W. Hess, Lattice Trapping Barriers to Brittle Fracture, Phys. Rev. Lett. **91**, 025501 (2003).
[14] S. Santucci, L. Vanel, and S. Ciliberto, Subcritical Statistics in Rupture of Fibrous Materials: Experiments and Model, Phys. Rev. Lett. **93**, 095505 (2004).
[15] L. I. Slepyan, Dynamics of a crack in a lattice, Sov. Phys. Dokl. **26**, 538 (1981).
[16] S. A. Kulakhmetova, V. A. Saraikin, and L. I. Slepyan, Plane problem of a crack in a lattice, Mechanics of Solids **19**, 101 (1984).
[17] L. Slepyan, Wave radiation in lattice fracture, Acoust. Phys. **56**, 962 (2010).
[18] L. de Arcangelis, A. Hansen, H. J. Herrmann, and S. Roux, Scaling laws in fracture, Phys. Rev. B **40**, 877 (1989).
[19] A. Hansen, E. L. Hinrichsen, and S. Roux, Roughness of Crack Interfaces, Phys. Rev. Lett. **66**, 2476 (1991).
[20] M. J. Alava, P. K. V. V. Nukala, and S. Zapperi, Statistical models of fracture, Adv. Phys. **55**, 349 (2006).
[21] S. Zapperi, A. Vespignani, and H. E. Stanley, Plasticity and avalanche behaviour in microfracturing phenomena, Nature (London) **388**, 658 (1997).
[22] See Supplemental Material at http://link.aps.org/supplemental/10.1103/PhysRevLett.123.205503, which includes (i) the determination of the Young's modulus in the three lattice geometry, (ii) the derivation of the William's expansion for the displacement or voltage field in the scalar antiplane elasticity problem, (iii) details on how to determine the crack-tip mispositioning with an arbitrary number of nodes, (v) details on the iterative procedure to determine this mispositioning, (vi) the detailed procedure to determine the crack tip mispositioning in a bidimensional crystal within the genuine planar stress tensorial elasticity problem, and (vii) its application to predict fracture toughness in graphene, which includes Ref. [23].
[23] F. Radjai, M. Jean, J.-J. Moreau, and S. Roux, Force Distributions in Dense Two-Dimensional Granular Systems, Phys. Rev. Lett. **77**, 274 (1996).
[24] *Structures, or Why Things Don't Fall Down*, edited by J. Gordon (Plenum, New York, 1978).
[25] M. L. Williams, Stress singularities resulting from various boundary conditions in angular corners of plates in extension, J. Appl. Mech. **19**, 526 (1952).
[26] J. Réthoré and R. Estevez, Identification of a cohesive zone model from digital images at the micron-scale, J. Mech. Phys. Solids **61**, 1407 (2013).

[27] R. Hamam, F. Hild, and S. Roux, Stress intensity factor gauging by digital image correlation: Application in cyclic fatigue, Strain **43**, 181 (2007).

[28] S. Roux and F. Hild, Stress intensity factor measurements from digital image correlation: post-processing and integrated approaches, Int. J. Fract. **140**, 141 (2006).

[29] B. C. Smith, *Infrared Spectral Interpretation: A Systematic Approach* (CRC Press, Boca Raton, 1999).

[30] C. Lee, X. Wei, J. W. Kysar, and J. Hone, Measurement of the elastic properties and intrinsic strength of monolayer graphene, Science **321**, 385 (2008).

[31] F. Liu, P. Ming, and J. Li, Ab initio calculation of ideal strength and phonon instability of graphene under tension, Phys. Rev. B **76**, 064120 (2007).

[32] J. Medina, F. Avilés, and A. Tapia, The bond force constants of graphene and benzene calculated by density functional theory, Mol. Phys. **113**, 1297 (2015).

[33] B. Xu, X. Gao, and Y. Tian, *Graphene Simulation* (InTech, Rijeka, 2011), Chap. Universal Quantification of Chemical Bond Strength and Its application to Low Dimensional Materials, pp. 211–226.

[34] P. Zhang, L. Ma, F. Fan, Z. Zeng, C. Peng, P. E. Loya, Z. Liu, Y. Gong, J. Zhang, X. Zhang *et al.*, Fracture toughness of graphene, Nat. Commun. **5**, 3782 (2014).

[35] J. Hutchinson, Singular behaviour at the end of a tensile crack in a hardening material, J. Mech. Phys. Solids **16**, 13 (1968).

[36] J. Rice and G. Rosengren, Plane strain deformation near a crack tip in a power-law hardening material, J. Mech. Phys. Solids **16**, 1 (1968).

[37] E. Bouchbinder, A. Livne, and J. Fineberg, The 1/r singularity in weakly nonlinear fracture mechanics, J. Mech. Phys. Solids **57**, 1568 (2009).

[38] J. Huang and L. Gibson, Fracture toughness of brittle honeycombs, Acta Metall. Mater. **39**, 1617 (1991).

[39] N. A. Fleck and X. Qiu, The damage tolerance of elastic-brittle, two-dimensional isotropic lattices, J. Mech. Phys. Solids **55**, 562 (2007).

[40] I. Quintana-Alonso and N. A. Fleck, Fracture of brittle lattice materials: A review, in *Major Accomplishments in Composite Materials and Sandwich Structures* (Springer, London, 2009), pp. 799–816.

[41] I. Quintana-Alonso, S. Mai, N. Fleck, D. Oakes, and M. Twigg, The fracture toughness of a cordierite square lattice, Acta Mater. **58**, 201 (2010).

[42] T. A. Schaedler, A. J. Jacobsen, A. Torrents, A. E. Sorensen, J. Lian, J. R. Greer, L. Valdevit, and W. B. Carter, Ultralight metallic microlattices, Science **334**, 962 (2011).

[43] D. Jang, L. R. Meza, F. Greer, and J. R. Greer, Fabrication and deformation of three-dimensional hollow ceramic nanostructures, Nat. Mater. **12**, 893 (2013).

[44] X. Zheng, H. Lee, T. H. Weisgraber, M. Shusteff, J. DeOtte, E. B. Duoss, J. D. Kuntz, M. M. Biener, Q. Ge, J. A. Jackson, S. O. Kucheyev, N. X. Fang, and C. M. Spadaccini, Ultralight, ultrastiff mechanical metamaterials, Science **344**, 1373 (2014).

[45] C. Huh and L. Scriven, Hydrodynamic model of steady movement of a solid/liquid/fluid contact line, J. Colloid Interface Sci. **35**, 85 (1971).